

Supplementary information of the paper

Improving free-energy estimates from unidirectional work measurements: theory and experiment

Matteo Palassini

*Departament de Física Fonamental, Facultat de Física,
Universitat de Barcelona, Diagonal 647, E-08028, Barcelona*

Felix Ritort

*Departament de Física Fonamental,
Facultat de Física, Universitat de Barcelona,
Diagonal 647, E-08028, Barcelona and
CIBER-BBN de Bioingeniería, Biomateriales y Nanomedicina,
Instituto de Salud Carlos III, Madrid*

(Dated: July 5, 2011)

Contents

1. Experimental details	3
1.1. Molecular synthesis of DNA sequences	3
1.2. Optical tweezers: measurements calibration and data acquisition	4
1.3. Work measurements	6
2. Analytical calculations	7
2.1. The bias in the high temperature regime, $\lambda \gg 1$	7
2.2. Extreme value statistics in the low temperature regime, $\lambda \ll 1$	8
2.3. The bias in the critical regime, $\lambda \simeq 1$	9
2.4. Numerical tests of the analytical approximations.	10
2.5. Corrections to the approximation $D_c = \mu$.	10
3. Further experiments illustrating the improved free energy estimator	12
3.1. Hairpin D (16 loop size)	12
3.2. Hairpins B,C (6,12 loop size)	13
4. On the Crooks fluctuation theorem and reconstructed WD tails	15
4.1. Test of the CFT in different hairpins	16
References	19

1. EXPERIMENTAL DETAILS

In what follows we briefly describe some details about the instrument, the experiments and the synthesis of the DNA molecules of varying loop size.

1.1. Molecular synthesis of DNA sequences

The molecular constructs used in this study consist of a DNA hairpin inserted between two flanking dsDNA handles of 29bp each. Recently we have shown that this molecular construct with short handles is much easier to synthesize than a construct with long handles and improves the signal-to-noise ratio of the measurements [1]. DNA constructs with short handles are synthesized using the hybridization of three different oligonucleotides (Fig. S1A). The first oligonucleotide contains the sequence of the ssDNA left handle plus a part of the sequence of the desired DNA hairpin; the second has the rest of the sequence of the DNA hairpin and the ssDNA right handle. The right and the left ssDNA handles have the same sequence to hybridize them with a third oligonucleotide called splint. The first oligonucleotide has a biotin at its 5' end and the second oligonucleotide has been modified at its 3' end with a digoxigenin tail (DIG Oligonucleotide Tailing Kit, 2nd generation, Roche Applied Science, Barcelona, Spain). Once the first and the second oligonucleotides are hybridized to form the hairpin, the third oligonucleotide is hybridized to the handles to form the dsDNA handles of 29 bp each. All the oligonucleotide sequences used in this construction are shown in Fig. S1B. The loop belongs to the second oligo and is underlined between parenthesis. Several loop sizes were investigated in this work ranging from 4 to 20 bases. Loops are of the type GAAA.. with a total number of A's equal to the size of the loop minus one. Hairpins A, B, C, D, E have loop sizes 4, 6, 12, 16, 20 respectively. An illustrative picture of the experimental setup is shown in Fig. S1c. The molecular construct is tethered to two beads through biotin-streptavidin and digoxigenin-antidigoxigenin connections. One bead is captured in the optical trap, the other bead is immobilized on the tip of a pipette. Experiments were done in aqueous buffer containing 10 mM Tris-HCl (pH 7.5), 1 mM EDTA, 500 mM NaCl and 0.01% Sodium Azide.

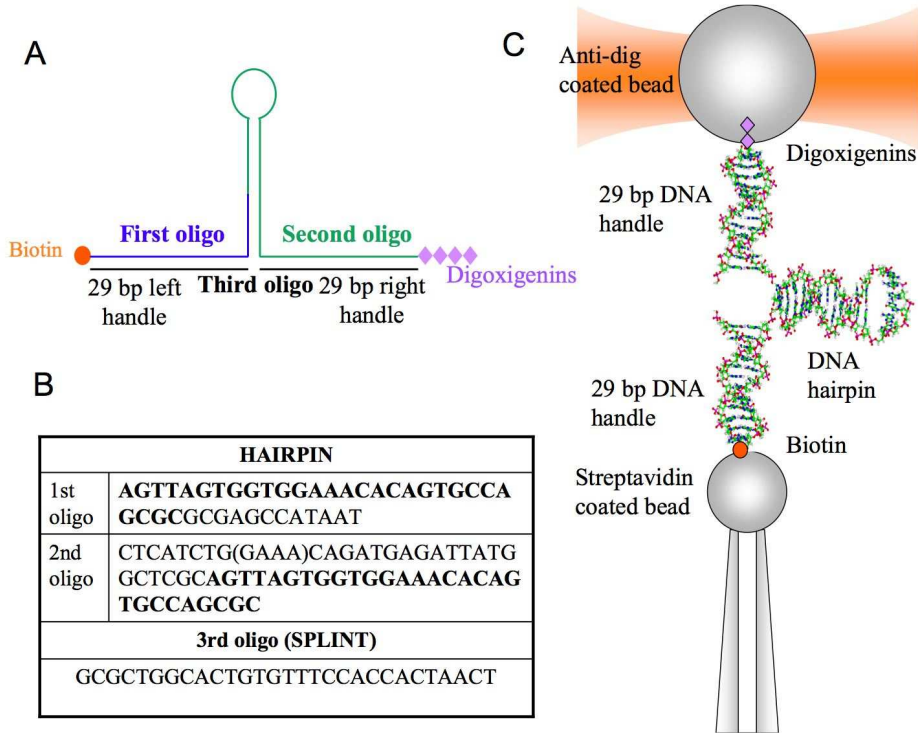


FIG. S1: **Molecular construct.** a) Schematics of the DNA synthesis. b) Oligo sequences. In bold face we show the base sequence that is complementary to the splint. Between parenthesis and underlined we show the loop GAAA... (a tetraloop GAAA in this case). c) Schematics of the experimental setup. Beads and DNA are not to scale.

1.2. Optical tweezers: measurements calibration and data acquisition

Fig. S2 shows the schematics of the miniaturized high stability optical tweezers instrument used in the experiments. It produces a single optical trap from counterpropagating laser beams [2]. By using low numerical aperture lenses and underfilling conditions the instrument directly measures forces by conservation of light momentum. The force is inferred by measuring the deflection of the scattered light by the bead. The offset of the deflected light is measured using a Position Sensitive Detector (PSD), and is converted into force by multiplying the photodetector signals by appropriate calibration factors. The force was calibrated using three different methods and all agree within a 5% error: power spectrum measurements, the Stokes law, and the equipartition theorem (see [2] for details). The distance measurements have a resolution of 1 nm which represents an uncertainty of about 3%.

The distance is measured with a light-lever. A small amount of the total light intensity of each beam (approximately 5%) is diverted from the main optical path just before it enters the focusing objectives and forms the optical trap. The diverted light is redirected to a Position Sensitive Detector (PSD) that measures the position of the center of the optical trap. The PSD is calibrated using a motorized stage with known pitch distance. The analog signals from the PSDs (position and force) are filtered using an analog low pass filter of bandwidth 1 kHz. The resulting signal is sampled at 4 kHz producing the raw data that we obtain in the experiment.

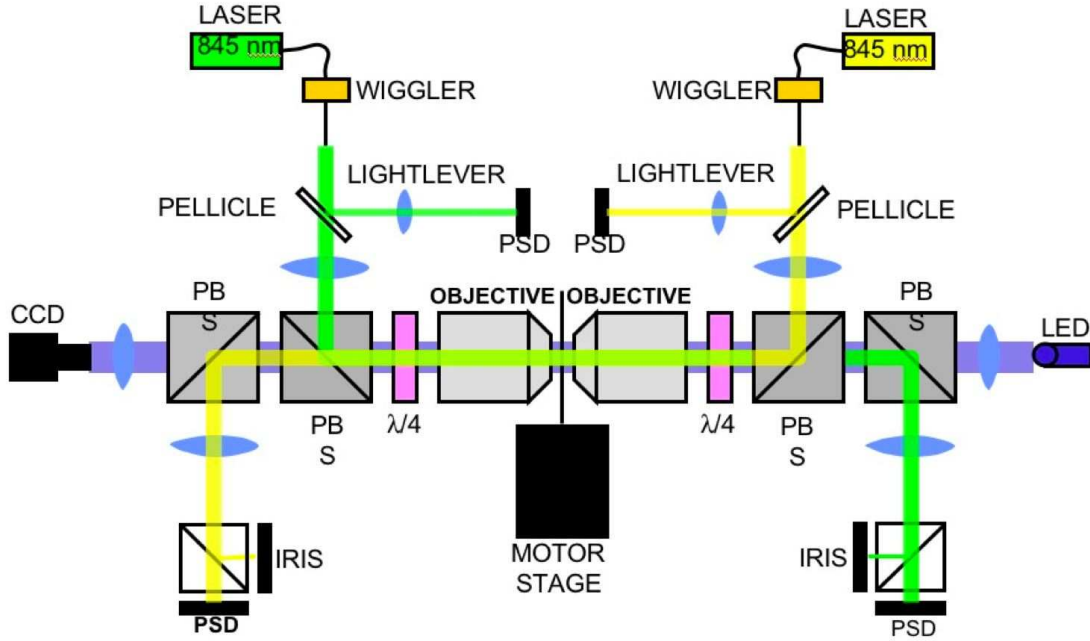


FIG. S2: **Minitweezers instrument.** Two optical fibers generate two counterpropagating beams (green and yellow) that are focused inside a fluidics chamber using low numerical aperture lenses. Lenses act as focusers and condensers by collecting the light of the two beams that is deflected by the bead in the trap. Polarized beam splitters and two quarter wave plates redirect the deflected light to Position Sensitive Detectors (PSDs) located at opposite sides of the instrument. PSDs are also used to determine the position of the optical trap along the plane that is perpendicular to the optical axis. A video imaging and Kohler illumination system (blue) are used to monitor the trapping experiment. The fluidic chamber is located between the objectives and can be moved by using a motorized stage. The instrument fits into a box, roughly weighs 5Kg and can be hanged from the ceiling.

1.3. Work measurements

We define X as the distance between the bead immobilized on the tip of micropipette and the center of the optical trap (see Fig. 1a for an illustration of how X is defined). This magnitude is a measurement that we collect directly from the instrument as the optical trap is moved up and down along the fluidics chamber. This is the control parameter in the experiment, i.e. the variable that does not fluctuate and the parameter that determines the statistical ensemble in our experiments (sometimes referred as mixed ensemble [3, 4]). Consequently, to measure work the appropriate representation of pulling curves is force versus relative trap-pipette distance, rather than molecular extension. In fact, the latter has been recently shown to induce, for high enough data acquisition frequencies, large systematic errors in extracting free energy differences using the Jarzynski equality [5]. Typical FDCs for hairpin A and work measurements are shown in Fig. S3.

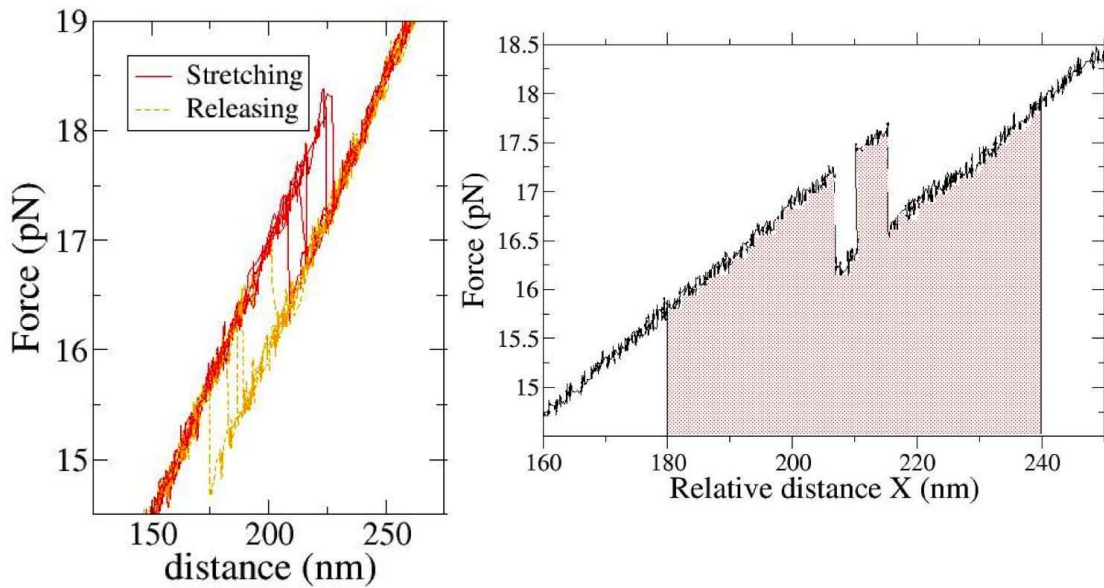


FIG. S3: (Left panel) Typical unfolding/refolding cycles for hairpin A pulled at approximately 200nm/s ($\simeq 8$ pN/s). FDCs exhibit hysteresis between the unfolding and refolding processes. (Right panel) The work for a given pulling curve is the area below the FDC between appropriate maximum and minimum distance limits. Work takes into account whether there are multiple unfolding and refoldings along a given curve (here we show two unfolding events and one refolding event during a single unfolding curve).

2. ANALYTICAL CALCULATIONS

In this section we describe in some detail the steps leading to the different analytical approximations for the generic WD introduced in main text. Let us express here the WD in terms of the dissipated work $D = W - \Delta F$,

$$p(D) \sim q \frac{\Omega^{\alpha-1}}{|D - D_c|^\alpha} \exp\left(-\frac{|D - D_c|^\delta}{\Omega^\delta}\right), \quad (1)$$

for which the Jarzynski equality (JE) can be rephrased as $\langle e^{-D} \rangle = 1$. The analytical results below are valid also without this constraint (which can be enforced simply by a shift of the mean), hence to express the results in a slightly more general form we keep the quantity $\langle e^{-D} \rangle$, which we require to be finite. This requires in general $\delta > 1$, which we assume here and in the main text. Note that the JE can also be satisfied with $\delta = 1$, $\Omega < 1$. This marginal case requires a separate analysis.

For $\delta > 1$, three regimes can be distinguished: a *high-temperature* regime where $\lambda \gg 1$, a *low-temperature* regime where $\lambda \ll 1$ and a *critical* regime where $\lambda \simeq 1$. Here “temperature” refers to the REM temperature, which we set equal to $(\log_2 N)^{(\delta-1)/\delta}/\Omega$, and should not be confused with the temperature T of the free-energy measurements. The regimes $\lambda \ll 1$ and $\lambda \simeq 1$ are the most relevant for biophysical studies where the average dissipated work $\langle D \rangle$ is large and the number of experiments N is not very large. A main result of our study is that the analytical expressions for either the low-temperature or critical regimes qualitatively reproduce our experimental results, depending on the experimental value of λ . In certain cases both expressions work well, when their region of validity overlaps.

2.1. The bias in the high temperature regime, $\lambda \gg 1$

Derrida [6] computed the corrections to the REM free energy in the case of the Gaussian distribution (GWD). The corrections computed by Derrida diverge at all integer values of λ , and thus cannot be directly applied to the data in Fig. 2 (main text). One can proceed instead as in Ref.[7], noting that for $\delta > 1$ the central limit theorem (CLT) holds for $\sum_i e^{-D_i}$. Thus from the theory of sums of random variables one obtains an Edgeworth series in N^{-1} ,

$$\langle B_N \rangle = \sum_{k=2}^{\infty} c_k \langle e^{-D} \rangle^{-k} N^{1-k} \quad (2)$$

where the coefficients c_k are polynomials in $\langle e^{-pD} \rangle$, $p \leq k$ [7]. This series is poorly behaved since $c_k \sim \exp[\mu(k^{\frac{\delta}{\delta-1}} - k)]$ grows very rapidly with k . In fact, as shown in Fig.S4 (top left panel) the leading term $c_2/N = \langle e^{-2D} - 1 \rangle / (2N)$, already considered in Refs.[8, 9], fits poorly the data for the GWD even for moderate values of Ω . The subleading term c_3/N^2 diverges below $\lambda \simeq 4$, and higher terms are even more divergent. Hence, truncating the series gives poor results.

Our approach is to resum partially the series. To this end, we make the key approximation of keeping only the most divergent term in each coefficient c_k . This gives the modified asymptotic series

$$\langle B_N \rangle = D_c - \mu + 1 - 1/(2N) - N \sum_{k=1}^{\infty} (-1)^{k-1} \langle e^{-kD} \rangle / (kN^k \langle e^{-D} \rangle^k), \quad (3)$$

which we are able to resum by exchanging the average and the sum [10], finding

$$\langle B_N \rangle = D_c - \mu + 1 - \frac{1}{2N} - N \langle \log \left(1 + \frac{e^{-D}}{N \langle e^{-D} \rangle} \right) \rangle. \quad (4)$$

We evaluate Eq.(4) for the GWD and the Weibull work distribution (WWD) by integrating numerically the last term $N \int dD p(D) \log(1 + e^{-D}/N \langle e^{-D} \rangle)$. As shown in Fig.S4, the agreement with the sampled data is very good for $\lambda \gtrsim 2$, improving vastly over the leading term $\langle e^{-2D} - 1 \rangle / (2N)$.

Let us also comment briefly on the case $\delta = 1$. For $\delta = 1$, $1/2 < \Omega < 1$, the CLT does not hold and one obtains $\langle B_N \rangle \sim N^{1-1/\Omega}$ [7]. For $\delta = 1, \Omega < 1/2$, the CLT holds but $\langle e^{-kD} \rangle$ is infinite for $k \geq \Omega^{-1}$, hence the power series for $\langle B_N \rangle$ is truncated at the largest k smaller than Ω^{-1} , and contains a term of order $O(N^{1-1/\Omega})$.

2.2. Extreme value statistics in the low temperature regime, $\lambda \ll 1$

For $\lambda \ll 1$, B_N will be dominated by the extreme value (EV) $M_N = \min_i \{D_i\}$, which is Gumbel-distributed for large N , i.e. $\text{Prob}(M_N < a_N + b_N x) \rightarrow 1 - \exp(-e^x)$ [11], where the coefficients a_N, b_N depend on the distribution $p(D)$. It is not too hard to compute the coefficients a_N, b_N for a distribution obeying Eq.(1), by which we obtain

$$\langle B_N \rangle \simeq \log N + \langle M_N \rangle \simeq \mathcal{B}_{\text{REM}} - \lambda^{\frac{1-\delta}{\delta}} \left[\gamma_E + \frac{1-\alpha-\delta}{\delta} \log \log N + \log(q/\delta) \right] \quad (5)$$

and $\gamma_E = 0.5772\dots$ is the Euler-Mascheroni constant. This is the expression given in Eq.(5) in the main text. This expression becomes asymptotically exact for large Ω and fixed $\lambda \ll 1$ but of course it fails at $\lambda = 0$ ($N = 1$).

2.3. The bias in the critical regime, $\lambda \simeq 1$

The critical regime $\lambda \simeq 1$ is technically more challenging. Cook and Derrida [15] were able to treat the GWD case with a traveling-wave (TW) approach, which we have extended to a generic WD with tail decaying as in Eq.(1). Using the identity

$$\langle \log Z_N(\beta) \rangle = \int_0^\infty dt t^{-1} [e^{-t} - e^{-I_N(\beta, -\beta^{-1} \log t)}], \quad (6)$$

where

$$I_N(\beta, x) \equiv -\log \langle \exp[-Z_N(\beta) e^{-\beta x}] \rangle = N \int dE p(E) [1 - \exp(-A)] \quad (7)$$

and

$$A = \exp[-\beta(x + E(\log_2 N)^{(\delta-1)/\delta})], \quad (8)$$

the problem of computing $\langle \log Z_N \rangle$ is translated in that of evaluating of $I_N(\beta, x)$ in the regime in which $I_N(\beta, x) \sim O(1)$. After some work, in this way we recover the EV result Eq.(5) above for $\lambda \ll 1$. For $\lambda \lesssim 1$ we obtain

$$\begin{aligned} \langle B_N \rangle \simeq \mathcal{B}_{\text{REM}} + \gamma_E - \lambda^{\frac{1-\delta}{\delta}} \left[\gamma_E + \frac{1-\alpha-\frac{\delta}{2}}{\delta} \log \log N \right. \\ \left. + \frac{1}{2} \log \frac{\pi q^2}{2\delta(\delta-1)} + \theta^2 + \log \text{Erfc}(\theta) \right], \end{aligned} \quad (9)$$

where Erfc is the complementary error function and

$$\theta = (\lambda^{\frac{1-\delta}{\delta}} - 1) \sqrt{\delta \log N} / \sqrt{2(\delta-1)}. \quad (10)$$

Eq.(9) corresponds to Eq.(6) in the main text. Although similar to Eq.(5), the two expressions tend to differ when λ is much smaller than one.

The region of validity of Eq.(9) is where $\lambda(\lambda^{(\delta-1)/\delta} - 1)^2$ is of order $O(\frac{2(\delta-1)}{\delta^{1/\delta} \Omega^{\delta/(\delta-1)})$. We can estimate this range approximately by treating this order-of-magnitude relation as an identity. For the typical values of Ω and δ found in our experiments we find in this way that the region of validity can extend to fairly small values of λ . When this is the case, both the critical and the low-temperature expressions quantitatively describe well the finite- N

correction to the bias. For example, for hairpins A, B, C shown in the lower panel of Fig. 2 (main text) we have $\delta = 2$ and $\Omega \in [2 - 8]k_B T$, thus the region of validity is $0.56 \lesssim \lambda \lesssim 1$ for the largest value of Ω ($\simeq 8k_B T$). The same point is illustrated in Fig.S4, where it can be seen that as Ω increases, the two regions of validity tend to overlap.

2.4. Numerical tests of the analytical approximations.

We tested Eqs.(4), (5) and (9) against the sampled data for the GWD and the WWD for many parameter combinations, some of which are shown in Fig. S4. We already remarked above the good agreement of Eq.(4) for $\lambda > 1$ and the poor behaviour of the truncated series. As can be seen in Fig. S4, both Eq.(5) and Eq.(9) agree well with the data in their domain of applicability ($\lambda \ll 1$, $\lambda \lesssim 1$ for Eq.(5),(9) respectively). For the GWD, we also show the power-law interpolation given by Eq.(7) in the main text. This expression also reproduces fairly well the data, although the agreement becomes worse as Ω increases.

2.5. Corrections to the approximation $D_c = \mu$.

Although Eqs.(5,9) give accurate expressions for the bias in the low-temperature and critical regimes, we still face the problem of predicting the free energy difference estimate ΔF . The improved free energy estimator ΔF_N^* discussed in the main text is based on the assumption that $B_N = \Delta F_N - \Delta F$, where ΔF_N is the Jarzynski estimator (Eq.2 in main text), is well represented by its mean $\langle B_N \rangle$, i.e. $\Delta F \approx \Delta F_N - \langle B_N \rangle$. (Of course B_N is a random variable, thus a more complete treatment would require to determine its whole distribution, not just the mean.) However, to implement this strategy we need to replace D_c in \mathcal{B}_{REM} (Eq.(5) in main text) by a quantity that can be expressed in terms of parameters obtainable from the measured WD, otherwise we would fall into a circular argument since $D_c = W_c - \Delta F$ contains ΔF itself. In the limit of large D_c we have shown that a saddle point calculation gives $\mu \simeq D_c$ to leading order. In order to estimate the error involved in the approximation $\mu = D_c$, we have numerically calculated μ for a WD given by Eq.(1) with $\alpha = 0$ for $D < D_c$, taking either $p(D) = 0$ for $D > D_c$ (asymmetric case) or $p(D)$ symmetric around D_c . Fig. S5 shows the difference $D_c - \mu$ versus D_c for both cases. Different curves correspond to different values of the exponent δ between one and two. As we can see,

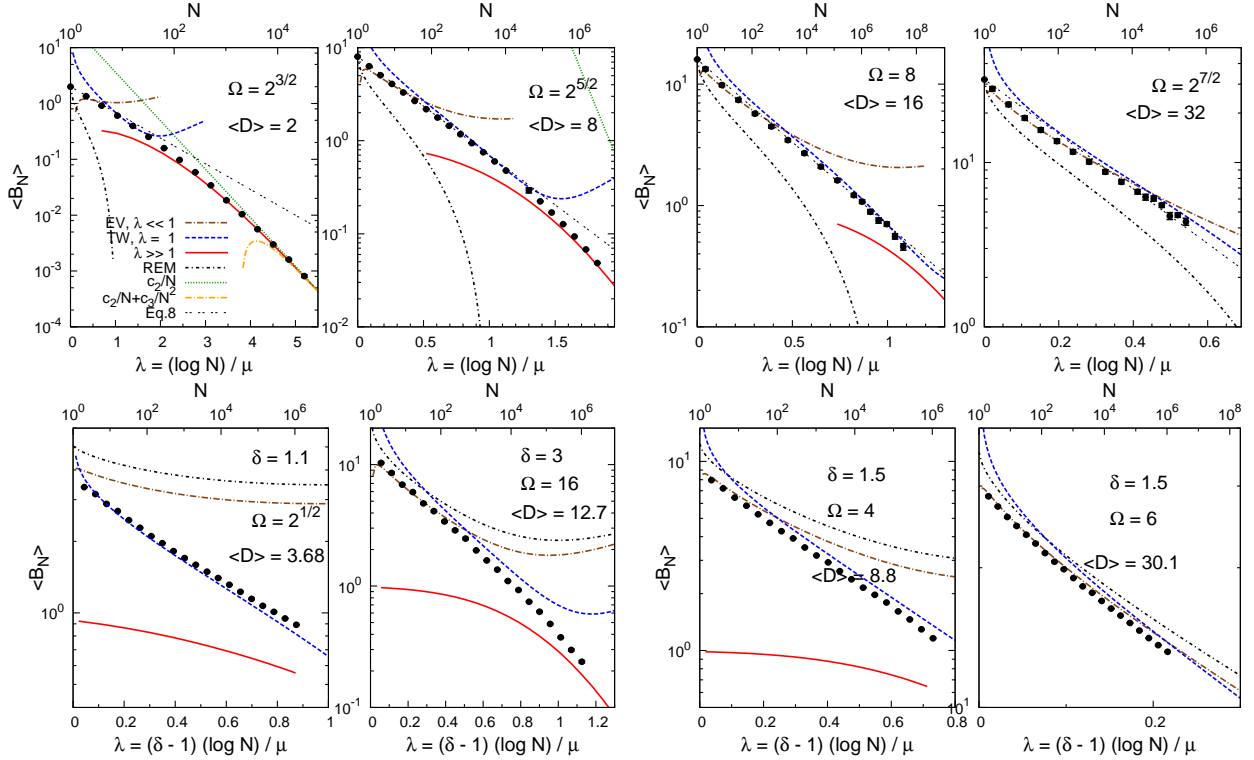


FIG. S4: Test of the analytical estimates of $\langle B_N \rangle$. The points are averages of B_N over many random sets (D_1, \dots, D_N) sampled from a GWD of variance $\Omega^2/2$ (top row) and a WWD (bottom row). The curves are our analytical estimates: Eq.(4) ($\lambda \gg 1$, continuous red line); Eq.(5) ($\lambda \ll 1$, dot-dashed brown line); Eq.(9) ($\lambda \lesssim 1$, dashed blue line); Eq.(7) of main text (light grey, long-dashed line). Also shown are \mathcal{B}_{REM} (Eq.(4) in main text, dot-dashed black line); $\langle e^{-2D} - 1 \rangle / (2N)$ (dotted green line); $\langle e^{-2D} - 1 \rangle / (2N) + c_3/N^2$ (dot-dashed yellow line), where c_3 is given in Ref.[7]. If some curves do not appear in some of the plots, it means that they fall outside the plot range.

the difference $D_c - \mu$ saturates to a limiting value as D_c increases. In particular we have $D_c - \mu < 0.7 k_B T$ for $\delta = 2$, and $D_c - \mu < 2.1 k_B T$ for $\delta = 1.5$. This small error justifies the validity of the approximation $D_c = \mu$ in the non-Gaussian WD case when D_c is large enough. This approximation has been used throughout this paper to extract free energy estimates (see Fig.3 in main text and Fig.S6). For the special case of a GWD the equality $D_c = \mu$ holds exactly.

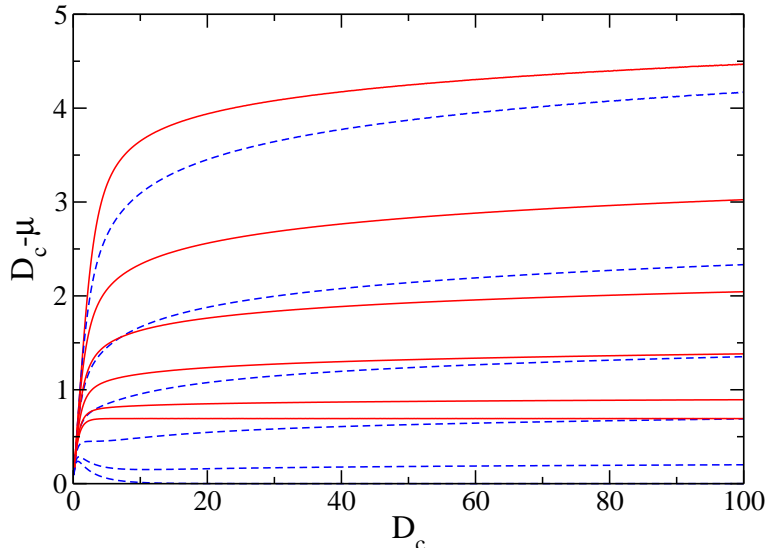


FIG. S5: **Corrections to the saddle point result** $D_c = \mu$. Different curves correspond to asymmetric WD (continuous red lines) and symmetric WD (dashed blue lines) as given by Eq.(1) with $\alpha = 0$. From top to bottom: $\delta = 1.1, 1.3, 1.5, 1.7, 1.9, 2.0$.

3. FURTHER EXPERIMENTS ILLUSTRATING THE IMPROVED FREE ENERGY ESTIMATOR

In this section we present further tests of the method introduced in the main text to extract improved estimates of free energy differences from unidirectional work measurements in two limiting situations: δ close to one (hairpin D) and δ close to two (the GWD case).

3.1. Hairpin D (16 loop size)

We investigated a hairpin with 16-bases loop where hysteresis is as large as for hairpin E (see Fig.1c of the main text for a qualitative comparison between FDCs). The results are summarized in Fig.S6. Hairpin D is particularly interesting because it exhibits asymmetric unfolding and refolding WD tails which are well fitted using an exponent δ close to one. As explained in the main text and in Section 4 below, in this situation we may expect that Eq.(1) cannot describe the tail over a large range of W values away from the region where experimental data are available. Indeed, the improved estimator in this case shows a marked dependence on δ , more so than for Hairpin E considered in the main text. This further illustrates that when δ is close to one, the method is not directly applicable without

additional information on the tail exponent for work values further out in the tails than the range measured experimentally.

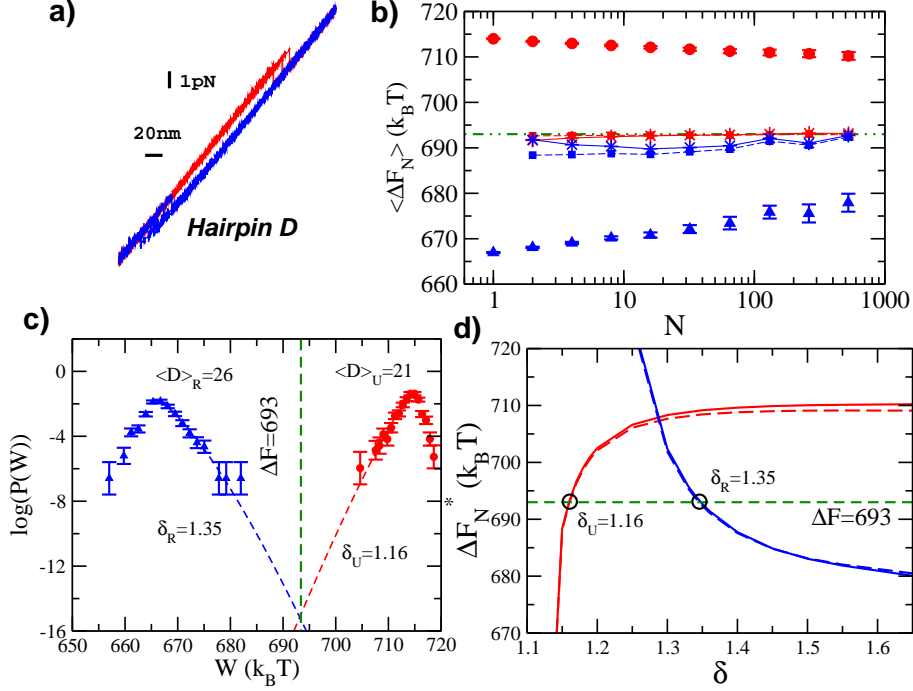


FIG. S6: **Free energy recovery for hairpin D.** (a) FDC cycles for hairpin D (16-bases loop) pulled at 200nm/s (same color code as in Fig.1 of the main text). Values of r are: 0.08 (U), 0.18 (R). (b) Jarzynski estimates are nearly flat exhibiting poor convergence. The improved estimators ΔF_N^* for $\delta_U = 1.16, \delta_R = 1.35$ converge to $\Delta F_{AR} = 693k_B T$ (dash-dotted line) for large N . Filled squares and stars correspond to ΔF_N^* calculated using Eqs.(5),(9) respectively. (c) WD in log-normal scale and recovered WD tails (dashed lines) and ΔF_{AR} value (vertical line). (d) Improved estimator ΔF_N^* as a function of δ for $N = 526$. The values of ΔF_N^* obtained using Eq.(5) (dashed lines) or Eq.(9) (continuous lines) are nearly indistinguishable for all δ . The circles indicate the values of δ_U, δ_R used in panel b).

3.2. Hairpins B,C (6,12 loop size)

To further illustrate that the improved estimator works well in the near-Gaussian case, in Fig. S7 we show results for Hairpin B and Hairpin C (the latter are the same data shown in Fig.1 of the main text). In these cases we can see that the improved estimator ΔF_N^* gives reliable results for exponent values $\delta \approx 2$.

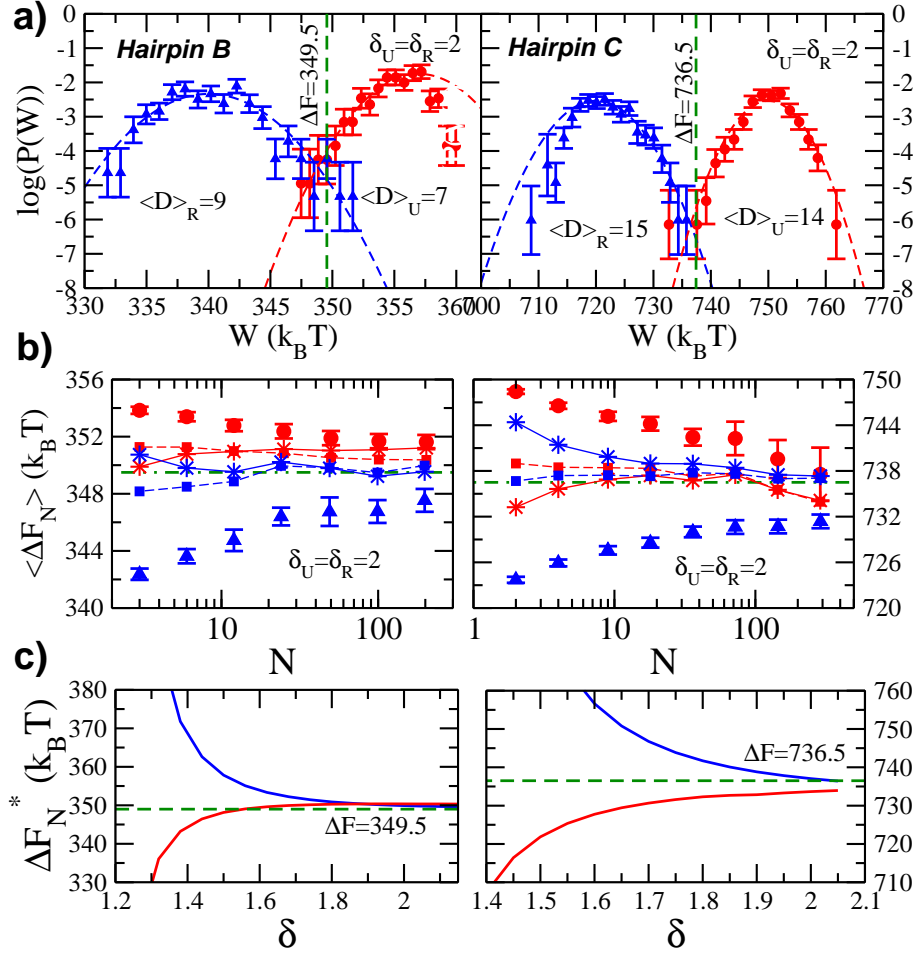


FIG. S7: **Free energy recovery for hairpins B and C.** Left panels correspond to hairpin B (200 nm/s and 203 cycles) and right panels to hairpin C (65 nm/s and 290 cycles). The values of r are 0.53 (U), 0.78 (R) for hairpin B and 0.67 (U), 0.81 (R) for hairpin C. **a)** WD in log-normal scale and GWD tails (dashed lines) and ΔF_{AR} value (vertical line). **b)** Jarzynski estimator (symbols) and improved estimator ΔF_N^* for $\delta_U = \delta_R = 2$ (symbols joined by lines). The latter converges to $\Delta F_{AR} \simeq 350 k_B T$ (dash-dotted line, left panel) and $\Delta F_{AR} \simeq 736 k_B T$ (dash-dotted line, right panel). Filled squares and stars correspond to Eqs.(5),(9) respectively. **c)** Improved estimator ΔF_N^* , obtained using Eq.(9), as a function of δ for $N = 203$ (left panel) and $N = 290$ (right panel). Note that ΔF_N^* converges to a value independent of δ as $\delta \rightarrow 2$. Hairpin B suggests values of δ_U slightly lower than 2 ($\simeq 1.7$) whereas $\delta_R \simeq 2$.

4. ON THE CROOKS FLUCTUATION THEOREM AND RECONSTRUCTED WD TAILS

The Crooks fluctuation theorem (CFT) expresses a symmetry between the forward and reverse WD, given by the relation

$$\frac{p_U(W)}{p_R(-W)} = \exp(W - \Delta F) \quad . \quad (11)$$

where both W and ΔF are expressed in units of $k_B T$. When both the forward and reverse WD are accessible, the best strategy to extract ΔF is to use them jointly and apply the CFT, and one way to do this in practice is to use the acceptance ratio estimator. The goal of the present work is instead to obtain better free energy estimates from *unidirectional* experiments where only one distribution is available. Therefore, the improved estimator does not use the CFT, which was used only to test the method a posteriori. Because we never used the CFT, we cannot guarantee that the fitted tails of the unfolding and refolding WD fulfill the symmetry neither in the vicinity of ΔF nor far away in the tails. In a previous work [13] one of us showed how a proper estimate of the free energy difference using the Jarzynski equality for the forward process, and viceversa, requires sampling work values around the most probable region for the corresponding reverse process. In fact, in the large W limit the free energy difference satisfies

$$\Delta F = W^\dagger - S(W^\dagger) \quad (12)$$

where $S(W) = \log(P(W))$ is the trajectory entropy [13] and W^\dagger and $S(W^\dagger)$ are given in $k_B T$ and k_B units, respectively. For the unfolding process W^\dagger satisfies,

$$\left(\frac{\partial \log(p_U(W))}{\partial W} \right)_{W=W^\dagger} = 1 \quad (13)$$

with the work W given in units of $k_B T$. Eq.(11) together with Eq.(13) implies,

$$\left(\frac{\partial \log(p_R(-W))}{\partial W} \right)_{W=W^\dagger} = 0 \quad (14)$$

meaning that $p_R(-W)$ is maximum for $W = W^\dagger$. Of course, an equation equivalent to (12) also holds for the refolding process. In other words, in order for the Jarzynski estimator for the unfolding work to have a negligible bias, unfolding work values around the maximum of $p_R(-W)$ must be sampled, and viceversa. When this is not possible because the dissipation

is too large, then, as discussed in the main text, if the lower tail of the unfolding WD can be fitted with $\delta \approx 2$, we expect that the improved estimator ΔF_N^* obtained using Eqs.(5,9) (that were derived by taking the generic function Eq.(1) as a faithful representation of the WD lower tail) will have a small bias. When δ is significantly smaller than two, then ΔF_N^* will systematically underestimate the true value of ΔF . This discrepancy is especially acute when $\delta \approx 1$ since in this case the lower tail of the WD does not match the reconstructed tail from the reverse WD. (By reconstructed $p_U(W)$ we mean here the distribution obtained from the measured $p_R(W)$ by applying the CFT, and viceversa.) In contrast, near-Gaussian distributions (with $\delta \approx 2$) tend to satisfy the CFT, and ΔF_N^* will be reliable using either Eqs.(5,9) with $\delta = 2$ or the interpolated formula Eq.(7) (main text).

4.1. Test of the CFT in different hairpins

Here we test whether the reconstructed tails satisfy the CFT, Eq.(11), for two non-Gaussian cases, hairpin E (Fig.3 of the main text) and hairpin D (Fig. S6), and two near-Gaussian cases, hairpins B and C (Fig. S7).

Hairpin D (Fig.S8, left panel) is characterized by unfolding and refolding WD tails well fitted by Eq.(1) with values of δ close to one. In this case, as previously explained, the fitted tails of the type Eq.(1) (red and blue continuous lines) do not satisfy the CFT. However, the fitted tails and the tails reconstructed from Eq.(11) (red and blue dashed lines) all cross around $\Delta F = 693k_B T$. The values for W^\dagger and $S(W^\dagger)$ for the fitted tails match well those corresponding to the true tails ($W^\dagger = 663, S(W^\dagger) = -43$ for unfolding and $W^\dagger = 717, S(W^\dagger) = -33$ for refolding).

Hairpin E (Fig.S8, right panel) is characterized by unfolding and refolding WD tails with larger values of δ than for hairpin D. In this case, fitted tails of the type Eq.(1) satisfy better the CFT. The fitted tails (red and blue continuous lines) and the tails reconstructed from Eq.(11) (red and blue dashed lines) cross around $\Delta F = 700k_B T$ and match each other reasonably well (certainly better than for hairpin D).

Hairpins B,C (Fig. S9) exhibit near-GWD and the experimental and reconstructed tails match each other reasonably well in the region delimited by the maxima of unfolding and refolding WD (i.e. by the values of W^\dagger corresponding to the unfolding and refolding processes, as given by Eq.(14)).

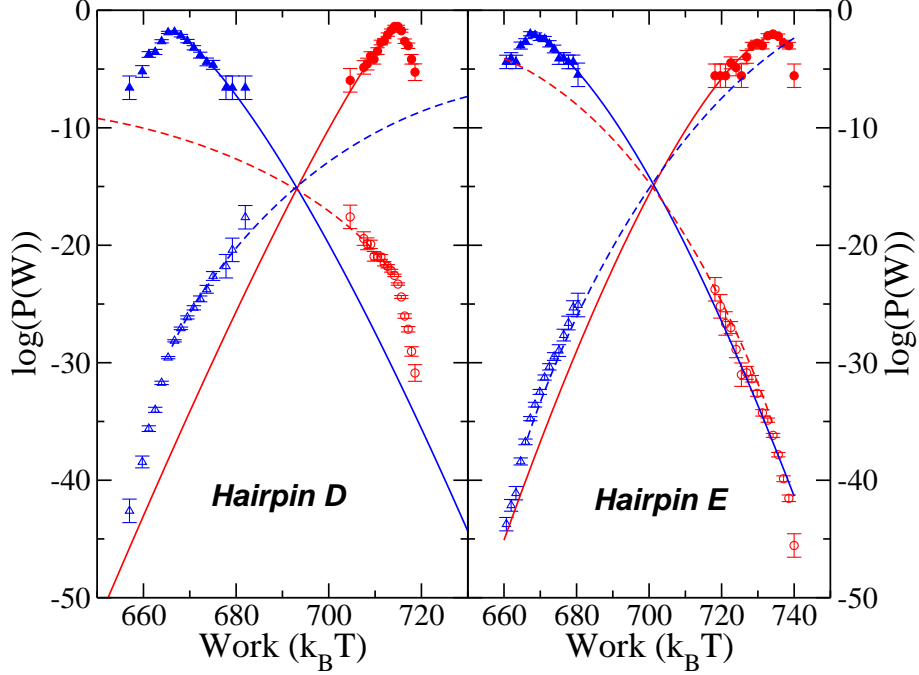


FIG. S8: **Testing the Crooks fluctuation theorem with reconstructed WD tails.** (Left panel) Hairpin D with 16-bases loop. (Right panel) Hairpin E with 20-bases loop. The filled symbols represent the unfolding (red circles) and refolding (blue triangles) experimentally measured WD's. The empty symbols represent the WD's reconstructed from the experimental WD's using Eq.(11). The fitted WD tails are shown as continuous lines for the unfolding WD (red) and the refolding WD (blue). The WD reconstructed from the fitted WD using Eq.(11) are obtained from the fits to are shown as dashed lines. Note that all lines cross around $\Delta F \simeq 693k_B T$ (hairpin D) and $\Delta F \simeq 700k_B T$ (hairpin E). The fact that the continuous red (blue) lines do not match with the corresponding dashed blue (red) lines indicates that the CFT Eq.(11) is not entirely satisfied by the generic WD Eq.(1). The discrepancy is particularly strong for hairpin D, which exhibits values of δ close to one ($\delta_U \simeq 1.16, \delta_R \simeq 1.35$) whereas it is only mild for hairpin E, which exhibits higher values of δ ($\delta_U \simeq 1.50, \delta_R \simeq 1.50$).

In summary, the WD may or may not be well modeled by Eq.(1) when δ is close to one. This will mostly depend on the form of the reverse WD which will determine whether the fitted WD satisfies Eq.(11) or it only describes the WD in a limited range of work values. In the latter case, the methodology presented in this paper can still be applied (see Fig. S6) provided the the reverse WD is known. Of course, if the reverse WD is known, then as we discussed the best strategy to estimate ΔF is to use the acceptance ratio

estimator which uses jointly the two distributions. When the tail exponent δ is larger than $\simeq 1.4 - 1.5$, our improved estimator provides a viable method to obtain free energies from unidirectional work measurements. Finally, we note that it is possible to devise alternative schemes to obtain improved free energy predictions from our analytical results, for instance by combining measurements taken at different irreversible conditions (e.g. varying pulling speed for the present type of experiments), by fitting the N dependence of the measured Jarzynski estimator, or using Bayesian inference techniques (for example, along the lines of Ref. [14]).

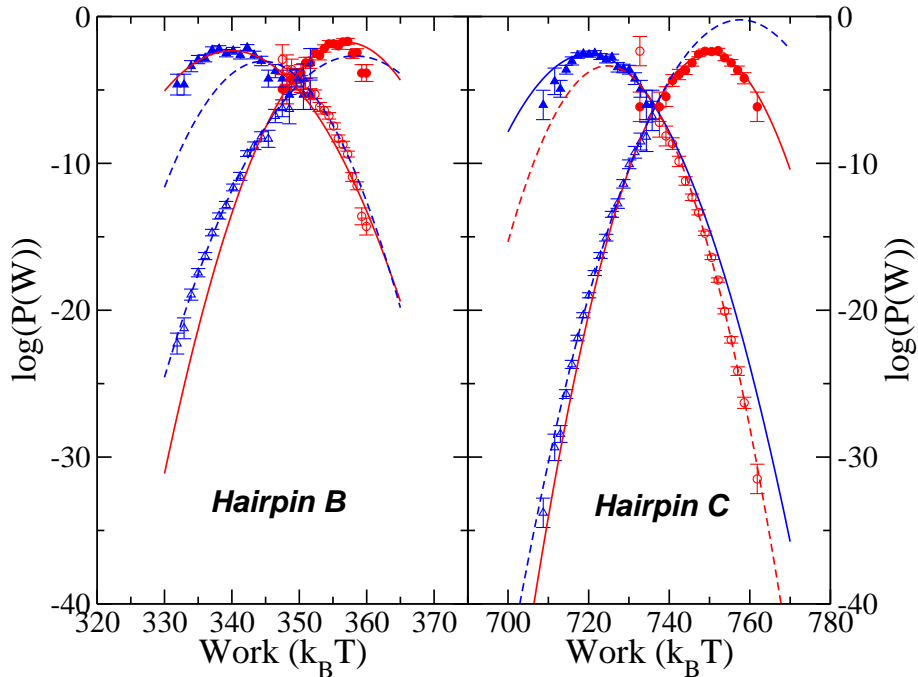


FIG. S9: **Testing the Crooks fluctuation theorem with reconstructed GWD tails** ($\delta_U = \delta_R = 2$). (Left panel) Hairpin B with 6-bases loop. (Right panel) Hairpin C with 12-bases loop. We show the unfolding (red circles) and refolding (blue triangles) experimentally measured WD (filled symbols). Empty symbols correspond to the matching experimental WD data using Eq.(11). The reconstructed WD tails are shown as continuous lines for the unfolding WD (red) and the refolding WD (blue). The corresponding matching tails are obtained from the Gaussian WD fits to the tails (continuous lines) using Eq.(11) and are shown as dashed lines. Note that all lines (continuous and dashed, red and blue) cross around $\Delta F \simeq 349.5k_B T$ (hairpin B) and $\Delta F \simeq 736.5k_B T$ (hairpin C). Continuous red (blue) lines match with the corresponding dashed blue (red) lines in the relevant work ranges (340-355 for hairpin B and 720-750 for hairpin C).

-
- [1] N. Forns, S. De Lorenzo, M. Manosas, K. Hayashi, J. M. Huguet, F. Ritort, *Biophys. J.* **100**, 1765-1774 (2011)
- [2] J. M. Huguet, C. V. Bizarro, N. Forns, S. B. Smith, C. Bustamante and F. Ritort, *PNAS* **107**, 15431 (2010).
- [3] U. Gerland, R. Bundschuh, and T. Hwa. *Biophys. J.* **81**, 1324 (2001)
- [4] M. Manosas and F. Ritort, *Biophys. J.* **88**, 3224 (2005)
- [5] A. Mossa, S. De Lorenzo, J. M. Huguet and F. Ritort. *J. Chem. Phys.* **130**, 234116 (2009)
- [6] B. Derrida, *Phys. Rev. B* **24**, 2613 (1981).
- [7] D. M. Zuckerman and T. B. Woolf, *Phys. Rev. Lett.* **89**, 180602 (2002); *J. Stat. Phys.* **114**, 1303 (2004).
- [8] R.H. Wood, W.F.C. Muhlbauer, and P.T. Thompson, *J. Phys. Chem.* **95**, 6670 (1991).
- [9] J. Gore, F. Ritort, and C. Bustamante, *PNAS* **100** 12564 (2003).
- [10] V. Dotsenko and M. Mézard, *J. Phys. A* **30** 3363 (1997).
- [11] J. Galambos, *The Asymptotic Theory of Extreme Order Statistics* (2nd ed.), Krieger, New York, 1987.
- [12] A. Mossa, M. Manosas, N. Forns, J. M. Huguet and F. Ritort, *J. Stat. Mech.* (2009) P02060
- [13] F. Ritort, *J. Stat. Mech.* P10016 (2004).
- [14] P. Maragakis, F. Ritort, C. Bustamante, M. Karplus and G. E. Crooks, *J. Chem. Phys.* **129**, 024102 (2008)
- [15] J. Cook and B. Derrida, *J. Stat. Phys.* **63**, 505 (1991).